Nuclear Instruments and Methods in Physics Research A 674 (2012) 28–38

Contents lists available at SciVerse ScienceDirect

Nuclear Instruments and Methods in Physics Research A

journal homepage: www.elsevier.com/locate/nima

A graphical tool for an analytical approach of scattering photons by the Compton effect

Francisco A. Scannavino Jr.[a,b,*], Paulo E. Cruvinel[a,b,*]

[a] Embrapa Agricultural Instrumentation Center, São Carlos, Brazil
[b] Physics Institute of São Carlos—IFSC, University of São Paulo, São Carlos, Brazil

ARTICLE INFO

Article history:
Received 24 August 2011
Received in revised form
11 November 2011
Accepted 27 December 2011
Available online 25 January 2012

Keywords:
Compton effect
Computer simulation
Graphical tool

ABSTRACT

The photons scattered by the Compton effect can be used to characterize the physical properties of a given sample due to the influence that the electron density exerts on the number of scattered photons. However, scattering measurements involve experimental and physical factors that must be carefully analyzed to predict uncertainty in the detection of Compton photons. This paper presents a method for the optimization of the geometrical parameters of an experimental arrangement for Compton scattering analysis, based on its relations with the energy and incident flux of the X-ray photons. In addition, the tool enables the statistical analysis of the information displayed and includes the coefficient of variation (*CV*) measurement for a comparative evaluation of the physical parameters of the model established for the simulation.

1. Introduction

The Compton effect is a phenomenon of interaction of X or gamma rays with the matter and its discovery has marked the evolution of classical physics into modern physics. It is still used as an example of a theoretical demonstration of relativistic quantum mechanics and quantum theory of fields. Such an effect demonstrates the angular distribution of radiation and scattered electrons as well as the shift in the frequency of the scattered photons.

It is important to observe that the Compton scattering is proportional to the electron density of the material under analysis. It is characterized by an inelastic event since there is energy loss. The photon shifts its initial path and an electron of the atom outer layer is removed from its orbit. However, due to the mass difference, an electron can never fully absorb the photon energy.

The relationship between the energy of an incident photon and that of a scattered photon is given by the equation:

$$\left(\frac{E}{E_0}\right) = \frac{1}{1+\alpha(1-\cos\theta)} \tag{1}$$

where E is the scattered photon energy [keV], E_0 is the incident photon energy [keV], α is the ratio between energy E_0 and the rest energy of an electron ($\cong 511$ keV) and θ is the scattering angle.

When a beam of monochromatic photons of incident energy E_0, in a photon flux Φ_0, interacts with a sample of homogeneous material of thickness x, the emergent flux Φ can be written as the Beer–Lambert equation:

$$\Phi = \Phi_0 e^{-\mu x} \tag{2}$$

where μ (cm^{-1}) is the linear attenuation coefficient for a material of physical density ρ (g/cm^3) and atomic number Z and x is the thickness of the sample.

For energy values over 10 keV, when the molecular binding energy is low, it is reasonable to assume that μ (cm^{-1}) is directly proportional to the physical density and therefore:

$$\Phi = \Phi_0 e^{-(\mu/\rho)\rho x} \tag{3}$$

where μ/ρ (cm^2/g) is the mass attenuation coefficient, which is proportional to the total cross-section per electron $\sigma_t^e(E)$ (cm^2/electron) as follows:

$$\frac{\mu}{\rho} = \frac{\sigma_t^e(E) Z N_A}{A} \tag{4}$$

where N_A is the Avogadro's number ($6.02 \times 10^{+23}$ atom/mol), Z is the atomic number and A is the material atomic mass. Therefore, the linear attenuation coefficient can be given by:

$$\mu = \frac{\rho \sigma_t^e(E) Z N_A}{A} \text{ or } \mu = \sigma_t^e(E)\left(\frac{\rho Z N_A}{A}\right). \tag{5}$$

* Corresponding authors at: Embrapa Agricultural Instrumentation Center and Physics Institute of São Carlos - IFSC, University of São Paulo. Rua XV de Novembro, 1452 13560-970 São Carlos, Brazil.
Tel.: +55 16 2107 2800; fax: +55 16 2107 2902.
E-mail addresses: scannavino@usp.br (F.A. Scannavino Jr.), cruvinel@cnpdia.embrapa.br (P.E. Cruvinel).

0168-9002
doi:10.1016/j.nima.2011.12.120

The electron density δ_e, which represents the number of electrons per cubic centimeter is given by:

$$\delta_e = \rho \frac{ZN_A}{A}. \quad (6)$$

Furthermore, substituting Eq. (6) into Eq. (5), the result leads to:

$$\mu = \sigma_t^e(E)\delta_e. \quad (7)$$

On the other hand, in a general way the total cross-section $\sigma_t^e(E)$ can be written as the addition of the different cross-sections contributions related to the manners of radiation interaction with the matter, given by:

$$\sigma_t^e(E) = \sigma_{ph}^e(E) + \sigma_C^e(E) + \sigma_R^e(E) + \sigma_{NI}^e(E) \quad (8)$$

where $\sigma_{ph}^e(E)$, $\sigma_C^e(E)$, $\sigma_R^e(E)$ and $\sigma_{NI}^e(E)$ represent, respectively, the cross-sections for the following effects: photoelectric [1–3], Compton scattering [4], Rayleigh scattering [5,6], and the nuclear interactions [7,8].

For the energy range between 10 and 300 keV, in which the probability of occurrence related to the Rayleigh scattering and the nuclear interactions is almost null in comparison with the predominant effects, these effects can be neglected. Therefore, Eq. (8) can be written as follows:

$$\sigma_t^e(E) \cong \sigma_{ph}^e(E) + \sigma_C^e(E). \quad (9)$$

Additionally, the photoelectric cross-section $\sigma_{ph}^e(E)$ [9] can be expressed by:

$$\sigma_{ph}^e(E) = \kappa Z_{ef}^3 \quad (10)$$

where κ is a constant.

By now, substituting Eq. (10) into Eq. (9), one has

$$\sigma_t^e(E) = \kappa Z_{ef}^3 + \sigma_C^e(E). \quad (11)$$

Additionally, substituting Eq. (11) into Eq. (7), it is possible to find:

$$\mu = [\kappa Z_{ef}^3 + \sigma_C^e(E)]\delta_e \text{ or } \mu = \delta_e[\kappa Z_{ef}^3 + \sigma_C^e(E)]. \quad (12)$$

In the energy range in which the Compton effect is prevalent, Eq. (12) can be written as:

$$\mu = \delta_e \sigma_c^e(E). \quad (13)$$

Besides, for a fixed energy and for non-hydrogen materials, Eq. (4) can be rewritten as:

$$\frac{\mu}{\rho} = \text{constant}, \quad (14)$$

demonstrating that the linear attenuation coefficient is only a function of the material physical density.

On the other hand, the Klein–Nishina cross-section [10,11] for a free electron is given uniquely by the relationship between the energy and the scattering angle:

$$\frac{d_e\sigma_{KN}(E)}{d\Omega} = \frac{r_0^2}{2}\left[\frac{1+\cos^2\theta}{(1+\alpha(1-\cos\theta))^2}\left[1+\frac{\alpha^2(1-\cos\theta)^2}{(1+\cos^2\theta)(1+\alpha(1-\cos\theta))}\right]\right] \quad (15)$$

where r_0 is the classical electron radius ($\cong 2.818\times10^{-13}$ cm) [12]. Eq. (15) is considered valid when the photon energy is much higher than the electrons binding energy of the sampled material.

The photon beam that reaches the sample is attenuated in the path between the source and the sample and also between the sample and the detector. The resulting count of scattered photons is given by:

$$S = \Phi_0 \exp\left(-\int_{x_1}\mu_1(x)dx - \int_{x_2}\mu_2(x)dx\right)\frac{d_e\sigma^{KN}}{d\Omega}\delta_e dV d\Omega \quad (16)$$

where μ_1 and μ_2 are the linear attenuation coefficients in the paths between source and sample (x_1) and sample and detector (x_2), respectively, dV is the scattering volume and $d\Omega$ is the detector field of view.

In 1988 and 1989, Hanson, Gigante and collaborators developed a mathematical method to visualize the geometry of the energy distribution scattering and also the angular variation of the Compton scattering related to the geometry of a given experimental arrangement [13–15]. The authors obtained constant scattering angles and constant scattered energy toroidal contours, by ignoring the absorption effects. They also highlighted the importance of observing the energy contours within a scattered volume, since they determine the magnitude of the geometric effects.

In 1992, Cesareo and co-authors published applications on techniques that used the interaction of photons (in keV range) with the matter [16]. Among these techniques, some research trends in the area of correlation between the Compton profile and the composition of the material under analysis were observed.

In 1993, Prettyman and collaborators described a visualization method of composition and density of industrial samples obtained through the combination of direct transmission tomography and a Compton scattering imaging system [17]. The dual-energy direct transmission tomography determined the map of linear attenuation coefficients, which provided a relationship between the effective atomic number and the effective atomic density. In this study, the Compton scattering imaging system determined a mapping of the sample electron density. The authors concluded that both theoretical results obtained by the Monte Carlo method through constructed projections and also by the experimental results presented good agreement and reliability to the parameters of the model developed to measure the response.

Also in 1993, Balogun and Spyrou investigated the influence that materials of high and low atomic number Z exert on Compton tomography images [18]. They used copper (Cu - low Z) and lead (Pb - high Z) and suited them in an aluminum (Al) phantom. The research showed that the edge could be faithfully reproduced depending on the difference of electron density between the two materials involved. Such a difference should be at least 60% higher or lower in function of the phantom composition material.

In 1994, Norton developed a technique for the reconstruction of tomographic images using the number of scattered photons detected as an energy function and also for the positioning of the detector [19]. The result was an electron density image that could be reconstructed from measurements of its line integrals over several overlapping circular paths. This result presented an analytical solution to the problem of idealized image reconstruction. The author emphasized that the Back-Projection Method was computationally efficient compared to methods based on the numerical inversion of large equation systems.

In 1997, Harding studied the Compton scatter imaging (CSI) and its applications to biomedical sciences and industry [20], emphasizing its important role in the contrast of radiographic images. Harding mentioned corrosion tests on aircraft fuselage, on radar satellite platforms and on sonar domes. He also analyzed preservation processes of mummified bodies in the biomedical area.

Also in 1997, Hubbell published a review about Compton scattering, validating the use of this as a function [21]. He concluded that, despite the necessary approximations, the Compton scattering factor was a useful tool for radiation transport and triple production calculations (pairs of electron–positron in the atomic electron field). Moreover, he highlighted that non-relativistic theoretical tabulations, produced by the Compton scattering function, showed accuracy to the order of 5% or higher for small

angles and for low and materials of medium atomic number. For larger angles and high atomic numbers, the values could reach accuracy of the order of 20%.

In 1999, Balogun conducted a numerical study on the variation of scattering angles and their influence on the scattered volume versus distance of the source-scattering center and different-sized collimators [22]. The author concluded that there was a certain symmetry between the volume at both forward and backward scattering angles in the range of $90^\circ \pm 30^\circ$. However a rapid increase in the scattering volume was observed in the angle configuration that exceeded 90° for both analyses (source-scattering distances and collimator sizes). He also highlighted that a low spatial resolution was observed for angles larger than 90°.

In 2000, Balogun and co-authors presented a numerical method to estimate the common volume of the intersection between two cones that represented the source and detector fields of view [23]. Additionally, they compared three methods: (i) one with a sequential scan of an elemental volume, presented as a paper in the previous year, (ii) a deterministic one and, (iii) another that uses the Monte Carlo technique. The authors concluded that the use of the Monte Carlo technique was efficient during the execution time in comparison with the two other methods and all the three algorithms converged to lower than 0.1% of the mean value.

In the same year, Cruvinel and Balogun built a dual-energy minitomography scanner for Compton scattering measurements used for agricultural applications [24]. The results showed a linear relationship between the size of soil aggregates and Compton measurement with a regression coefficient better than 0.95 for the bulk density and 0.70 for water content. The minimum detected density was $0.13\ g/cm^3$ and the minimum detected moisture was $0.10\ cm^3/cm^3$, corresponding to 2% and 5% of precision, respectively.

Also in 2000, Yalçin and collaborators used a gamma ray energy source (^{241}Am) corresponding to 59.5 keV and a Ge-type (Li) detector positioned in a scattering angle of 110° to analyze the Compton scattering functions of some chemical elements, such as aluminum (Al), iron (Fe), nickel (Ni) [25]. The experimental results showed an error rate of less than 11% and good agreement with the theoretical values.

In 2001 and 2002, Cesareo and co-authors designed and built an instrument to measure and to image samples through X-ray scattering [26]. The authors conducted studies on Compton and Rayleigh scattered radiation, including Compton profile measurements through an X-ray tube and a semiconductor detector. The experimental values were in accordance with the theoretical ones. In 2002, Cesareo and collaborators built a first-generation tomograph to measure photons through Compton scattering [27]. The authors emphasized that the main advantages obtained by Compton tomography were (i) measurements of objects which were not accessible in all directions and (ii) a good contrast between the air and the material, at least theoretically. The disadvantages were (i) a lower count of photons due to the object-detector solid angle, in which greater energy X-ray tubes were needed and (ii) multiple scattering within the object, which reduces the image quality.

In 2003, Balogun and Cruvinel used Compton tomography to analyze the compaction of agricultural soils [28]. They used a defined-volume soil sample to obtain images of the soil density distribution through the number of photons identified by Compton scattering. The tomographic images obtained were presented with resolution, shape and edge definition contrasts. The authors highlighted that in order to obtain a higher level of both efficiency when detecting photons and spatial resolution, a focusing collimator was necessary to partially compensate the low cross-section for the Compton effect. In tomography with Compton scattering photons, the choice of scattered energy was given by the scattering angle, the materials to be analyzed and the size or the depth of the sample. According to the authors, in some applications, as soil analysis, the use of low energy photons (≤ 60 keV) was indicated for studies of surface phenomena, like soil sealing. When deep knowledge was required, as in soil compaction, higher-energy photons favored the analysis.

In the context of simulation tool and software for physical experimental setups, also in 2003, Agostinelli and co-workers developed a simulation computational tool called GEANT4—a simulation toolkit [29]. The software simulated the passage of particles through the matter and presented a broad set of functions, such as tracking, geometry, physical models and collision. Some physical processes, like electromagnetic and optical ones, were available in the tool. In addition, a large set of particles, materials and elements over a wide starting energy range (from 250 keV to 1 TeV) were also available.

In 2004, Roy and Pratt compared the Klein–Nishina cross-section theory with the measurements (from 11 to 40 keV) of the whole atom and used a synchrotron-type X-ray source [30]. The results showed the experimental comparison of the cross sections measured by both conventional and synchrotron sources and by using the predicted values of the Incoherent Scattering Factor (ISF). The measurements performed with conventional sources were scattered, with the ISF magnitude difference ranging from 5% to 50%, while the measurements taken by the synchrotron source showed a low difference in percentage. In order to confirm the adequacy of the theoretical treatment, the authors highlighted the importance of working not only with Compton scattering measurements in the range below 10 keV, but also with a greater number of work using angles different from 90° and different atomic number Z values.

In the same year, Söğüt and collaborators investigated the dependence on the average atomic number of coherent/incoherent scattering intensity ratio in molecules. The source used provided 59.5 keV of gamma rays [31]. They observed that the intensity of Rayleigh/Compton scattering was directly proportional to the increase in the effective atomic number.

Also in 2004, Rao and co-authors have obtained results ranging from 5 keV to 10 MeV in the Klein–Nishina cross-section for subshells of 12 biologically interesting chemical elements [32]. The data generated were used for simulating photon transport within the matter. The cross-sections for the complete atom obtained after summing the subshells data and the results have been in accordance with the previous values.

In 2005, Çonka-Nurdan and co-authors developed a system using a coincidence Compton camera (Anger-type) with a silicon drift detector [33]. It was constructed to study coincidence events and the possibility of tracking a recoil electron. The measurements could be performed in all the detector orientations and kinematic conditions.

In 2006, Cruvinel and Balogun applied Compton scattering tomography to analyze the density and the content of water in soils [34]. The quantitative results were obtained through the application of the reconstruction algorithm, which took the absorption of incident and scattered radiation into account. The authors compared the values of linear attenuation coefficients in soil density measurements with the Compton and the direct transmission techniques, obtaining a correlation factor of 0.81. For measurements of water content, the correlation factor obtained was 0.79. However, they compared the Compton technique with the Time Domain Reflectometry (TDR) technique.

Also in 2006, Pašić and Ilakovac measured the Compton scattering to investigate the Compton scattering function by the Coincidence Method for outer layer electrons [35]. The data on the double-differential Compton scattering cross-sections with

energy ranging from 60 to 105 keV and those obtained through the approximation of non-relativistic impulse were in conformity with the data obtained by the coincidence method.

In 2007, Donativi and co-authors analyzed chemical elements and compounds that presented low atomic number Z $(5-12)$ using scattered and monochromatic radiation, but with Rayleigh/Compton (R/C) ratio information approach [36]. The authors used the R/C ratio instead of analyzing Rayleigh and Compton effects separately, because the ratio was dependent on neither the geometric arrangement nor the material physical density, but on high powers of Z and could characterize and identify materials with low Z values. Using an X-ray tube and a detector positioned at a 90° scattering angle, the results showed accordance with the theoretical and practical values. The results demonstrated that the technique was a good alternative for measuring materials that presented low Z values and similar linear attenuation coefficients.

In the same year, Seo and collaborators used images obtained by a double-scattering Compton camera (DOCI – Double-Scattering Compton Imager) together with the GEANT4 simulation software [37] by the Monte Carlo method. The simulation model included the detector geometric details, the energy resolution, the spatial resolution and the discrimination levels of both source energy and detector. The aim was to improve the efficiency and the resolution of the Compton camera using two detectors as scatterers, instead of one, and one detector as the absorber. The scatterers had to locate the Compton scattering and the energy deposited in the process, while the absorber had to determine the location and the energy of the photon absorbed. The results showed a significant increase in the Compton camera resolution with the use of two scatterers; however the efficiency obtained was still considered low, approximately 10% in comparison with the system of a scatterer. The authors reported that such efficiency could be improved by placing multiple high-resolution detectors for each of the two scatterer detectors.

In 2008, these authors modified the geometric configuration with the double-scattering Compton camera in an attempt to maximize its efficiency [38]. After a simulation with the GEANT4 software, two scatterer detectors were placed in parallel and 8 cm apart from each other. For gamma ray energy of approximately 500 keV, the results showed an image resolution of 8.6 mm (FWHM—Full Width at Half Maximum) and a sensitivity of 1.3×10^{-7}. In addition, the authors highlighted that the simulation indicated the Compton camera would perform better in this case and could be used for PET (Positron Emission Tomography) tomographic image applications for analyses of the human body.

In 2009, Yao and Leszczynski presented an analytical approach to approximately separate the unknown information of the Klein–Nishina cross-section formula and express them through the primary intensity of X-rays in the detector [39]. The approach was compared with the exact solution of the Klein–Nishina cross-section and the simulations performed using the Monte Carlo method. The result showed that the approximate relation between the first-order scattering and the primary intensity fluence in the detector was useful to estimate the scattered radiation on physical projections from a phantom.

In the same year, Hartemann published a review on linear and nonlinear Compton scattering compared with Thomson scattering [40]. The author pointed out that two distinct processes played important roles in the nonlinear regime, namely multi-photon interactions and the radiation pressure. Both phenomena influenced the source brightness, demanding different modeling strategies.

In 2010, Pratt and co-authors wrote a literature review describing the recent findings on the Compton scattering of bound electrons [41]. The authors highlighted the advances of the Compton scattering theory and drew particular attention to the Impulse Approximation technique, which provided a broad description of the Compton effect on its peak region.

Also in 2010, Pires and co-authors published a literature review of the last 25 years of computed tomography in Brazil for the analysis of soil physics [42]. Among the tomography techniques, they pointed out the results obtained by Compton effect tomography for the analysis of soil density based on the results published by Cruvinel and collaborators.

The present paper describes a tool for an analytical approach of the Compton effect. It enables a graphic display of information on photon scattering to aid the decision-making process of defining experimental arrangements. The main contribution of this work concerns the visual and quantitative analysis of photons scattered by the Compton effect by inserting data to the Compton photon detection equation. The time window, the detector efficiency in the photopeak energy, as well as its position, the energy and the flux of incident photons can be used as data for a graphic display of Compton photon variations. Such approach enables a more realistic understanding of the experimental behavior of the photons scattered by the Compton effect.

2. Materials and methods

To validate the method, a case study was used considering: (i) an X-ray source for energy values between 0.5 and 100 keV and photon flux variation of 1 k to 150 k, (ii) a detector efficiency of 2% in the photopeak region, (iii) time window varying from 10 to 100 s, with an increment of 10 s from the initial value, (iv) the chemical compound silicon dioxide (SiO_2) as a sample, which presents physical density (ρ) equal to 2.32 g/cm^3, effective atomic number (Z_{ef}) equal to 11.56 atom/mol and molar mass equal to 60.07 g/mol, and (v) a geometric arrangement for experiments using the Compton effect.

The geometrical arrangement parameters used in this case study were: (i) positioning of the detector (scattering angle (θ)) ranging from 0 to 180°, (ii) a 5.40 cm wide by 5.40 cm long phantom and (iii) distance from the phantom wall to its center (x_1') equal to 2.70 cm.

The Compton scattering takes into account the following items: experimental design, type of material under analysis, technical characteristics of both Gamma and X-ray sources, and detectors. Fig. 1 presents the geometrical arrangement used for the simulation.

In Fig. 1, it is possible to notice that the source and the detector fields of view are cone-shaped (source - straight lines s and t, detector - straight lines r and n). The intersection of both cones, whose limits are given by points Z_1, Z_2, Z_3 and Z_4, generates a volume called cone intersection volume of the fields of view. The detected photons are generated by photon–electron collisions within this intersection volume. The detector positioning, after choosing the scattering angle θ, determines the Compton cross-section and the energy of scattered photons. The diameters of the source and the detector collimators along with their lengths determine the half-angles ψ and β, which consequently influence the intersection volume. In this work, the linear attenuation coefficient of the air has been neglected, due to its low value in a broad range of energies. Therefore, distances x_1 and x_2, given in Eq. (16) as the distances between the source-sample and the sample-detector, respectively, become the distances traveled by the photons within the sample.

In this simulation, only the linear attenuation coefficients (μ) and the material within the phantom, related to the incidence (μ_1) and the scattering energy (μ_2), have been taken into account. Due to its quadratic form, the choice of angle θ influenced the distance traveled by the Compton photon within the sample (x_2').

The distance traveled by incident photon traveled (x_1') was constant because not changed the source position and its value was the same as half of the phantom length value ($cp/2$).

XCOM software [43] allowed obtaining the linear attenuation coefficient values by selecting the energy range of scattered or incident photons, the data on chemical formulations or the element symbol in the periodic table and physical density of the element or chemical compound.

The organized modeling for the photon scattering simulation by the Compton effect was based on the general photon detection equation (Eq.(16)), however including two new terms for a more realistic approach [24]. The two terms that contribute to the amount of photons detected were time window in second t and detector efficiency ε in the photopeak energy region. By adding these terms into Eq. (16), it can be rewritten as:

$$S(E) = \Phi_0 \varepsilon t \exp\left(-\int_{x_1'} \mu_1(x)dx - \int_{x_2'} \mu_2(x)dx\right) \frac{d_e \sigma^{KN}}{d\Omega} \delta_e dV d\Omega. \quad (17)$$

The contribution of the linear attenuation coefficient with the incident and the scattering energies in Eq. (17) was named linear attenuation factor ($cfat(\mu, x)$) and the differential Klein–Nishina cross-section (Eq. (10)) was named *KN*.

The linear attenuation coefficient factor ($cfat(\mu, x)$) is given by equation:

$$cfat(\mu,x) = \exp\left(-\int_{x_1'} \mu_1(x)dx - \int_{x_2'} \mu_2(x)dx\right). \quad (18)$$

In addition, Eq. (17) has been normalized to both volume unit dV and differential solid angle unit $d\Omega$, resulting in:

$$\frac{S(E)}{dV d\Omega} = \Phi_0 t \varepsilon cfat(\mu,x) KN \delta_e \quad (19)$$

where the resulting value is given in photons/(sr cm^3).

Using Eq. (19), the simulation can be conducted in three stages: (i) scattering angle variation ($\Delta\theta$), (ii) energy variation of incident photons (ΔE_0) and (iii) flux variation of incident photons ($\Delta\Phi_0$).

Fig. 2 illustrates the block diagram of the developed model for the analytical approach of the Compton effect visual characterization, which has been implemented in Matlab (MathWorks). It also shows the geometric arrangement and the parameters used for the model established for the simulation process.

Once the element or chemical compound has been chosen, one determines either the atomic number Z (element) or the effective atomic number Z_{ef} (compound), the physical density of the material (ρ) and the atomic mass A (element) or molar mass A_m (compound) based on the values in the literature. The electron density (δ_e) is calculated using values of Z or Z_{ef}, A or A_m, ρ and the value of the Avogadro's number N_A.

The incident photon energy (E_0) determines the energy of the Compton photons (E) together with the choice of the scattering angle (θ) and the ratio between energy E_0 and the rest energy of the electron (*alf*). The choice of angle θ determines the path traveled by the scattered photon (x_2') within the quadratic phantom and also the Klein–Nishina cross-section (*KN*). Variable

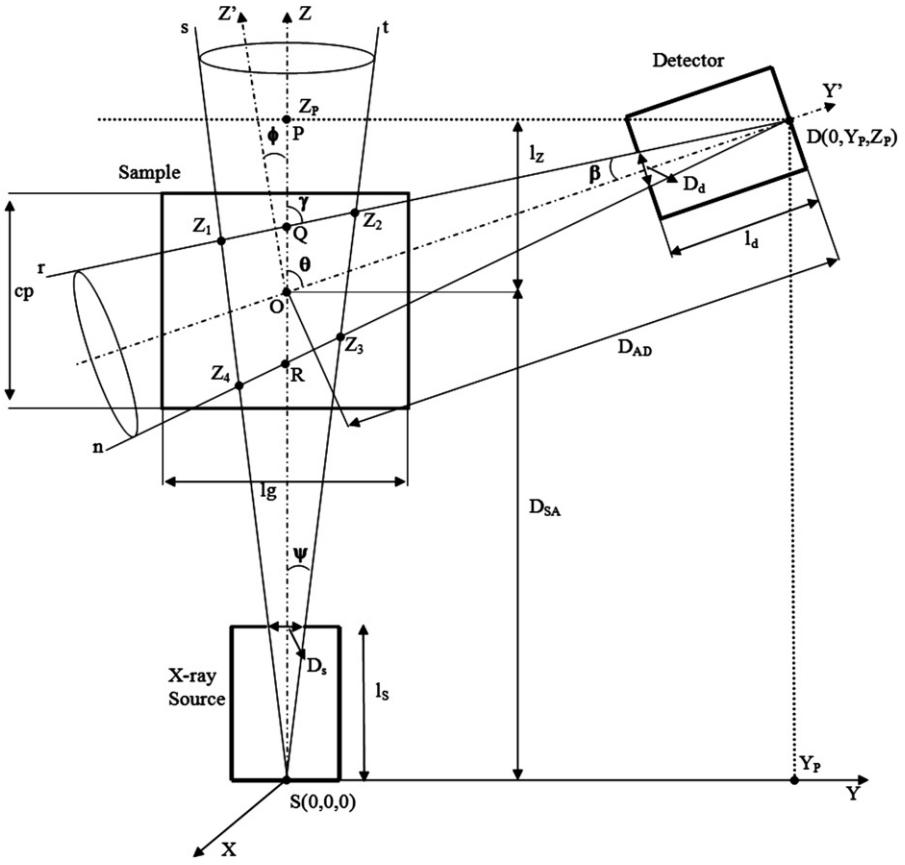

Fig. 1. A typical geometric arrangement used for experiments on Compton scattering. Variables Z_1, Z_2, Z_3 and Z_4 represent the intersection limits of both source and detector fields of view, θ is the scattering angle, ψ and β are the source and detector aperture, respectively, l_g and c_p represent the phantom width and length, respectively, l_s and l_d represent the source and the detector length, respectively, D_s and D_d represent the diameters of the source and the detector collimators, respectively, D_{SA} and D_{AD} indicate the source-sample center and the sample center-detector distances, respectively, l_z is the distance between the center of the sample and the Z-axis coordinate of the detector, O is the center of the sample, x_1' is the distance (cm) traveled by the incident photon within the sample and x_2' is the distance traveled by the scattered photon within the sample.

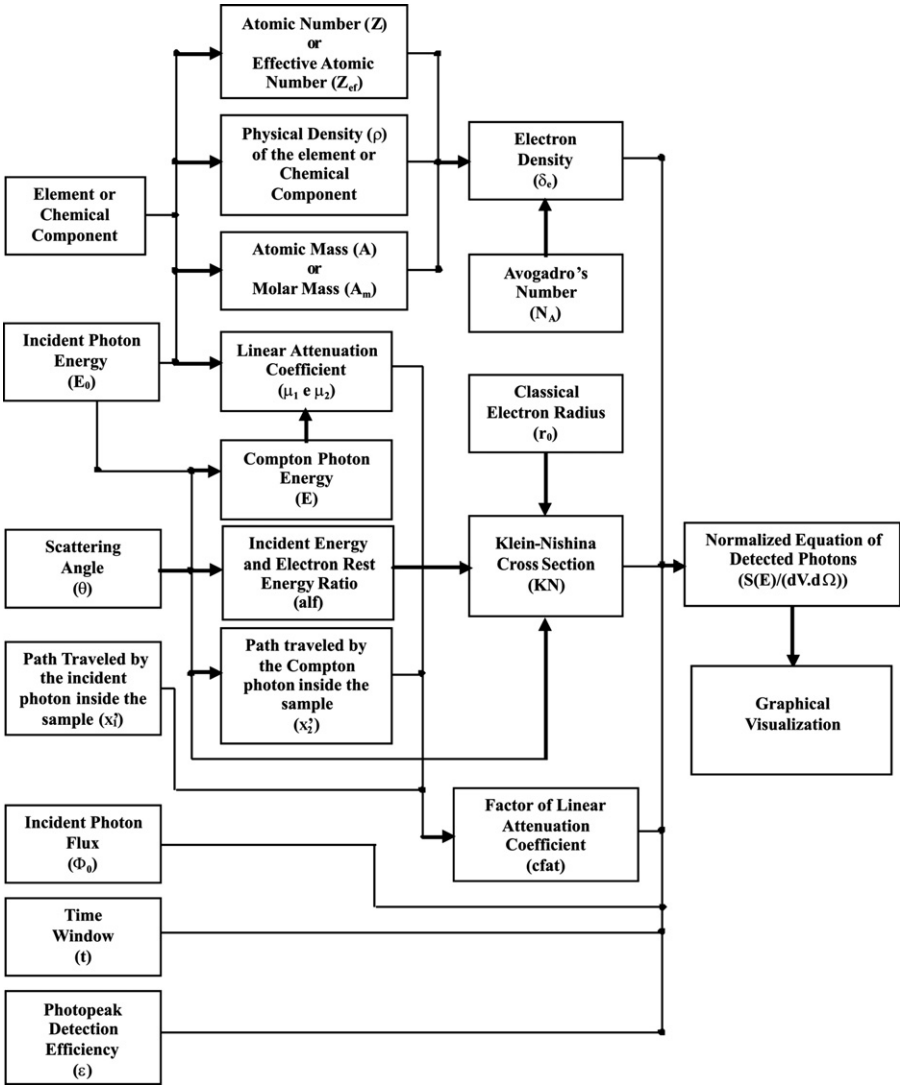

Fig. 2. Block diagram of the analytical approach model for the Compton effect with visual characterization.

KN also uses the values of both classical electron radius (2.82×10^{-13} cm) and variable *alf*. The linear coefficient factor (*cfat*) uses the values of the path traveled by the incident photon (x_1') and the scattered photon (x_2'), the linear attenuation coefficients for incident (μ_1) and Compton energy (μ_2). The normalized equation for the detected photons uses the values of the time window (t), the incident photon flux (Φ_0), the detector efficiency in the photopeak region (ε) and variables δ_e, *KN* and *cfat*.

Fig. 3 shows the tool output for both graphical and analytical approaches on the scattering of photons by the Compton effect.

The graphical output produced by the tool illustrates the variation of the scattering of photons by the Compton effect using input parameters, such as energy (E_0) and flux of incident photons (Φ_0) and scattering angle (θ), which determines the energy of the scattered photons that reach the detector. The results produced graphically are presented through statistical parameters such as variance (σ_d^2), standard deviation (σ_d) and coefficient of variation (*CV*).

3. Results and discussion

For the case study, the validation results of the simulation model developed have been presented in four graphical outputs: (i) polar graphics for scattering angle variation ($\Delta\theta$) ranging from 0 to 180°, (ii) semi-logarithmic graphics for energy variation (ΔE_0) of incident photon ranging from 0.5 to100 keV, (iii) linear graphics for the variation of incident photon flux ($\Delta\Phi_0$) ranging from 1 k to 150 k photons/cm^2 and per seconds and (iv) statistical parameter tables of the results obtained through scattering angle variation, the energy and the flux of incident photons in relation to the amount of scattered photons per volume unit and per solid angle unit (Fig. 3).

The variation of the distance traveled by the Compton photon within the phantom (x_2') is illustrated in Fig. 4. This figure shows that, for a quadratic phantom, the photon path distance is strongly dependent on the position of the detector. Considering the phantom center, the phantom diagonals are located at 45° and 135°. In a circular phantom, this distance would be a constant of the value equivalent to the circle radius.

The linear attenuation coefficient factor has shown that there were correlations with distances x_1' and x_2', respectively, for μ_1 and μ_2. Variable x_1' has a constant value since the X-ray source does not move. On the other hand, the variation of the detector positioning given by the scattering angle (θ) influenced the variation of variables x_2' and μ_2', as well as *cfat*.

Fig. 5 shows how the phantom shape can influence the linear attenuation coefficient factor (*cfat*). The angle position of the

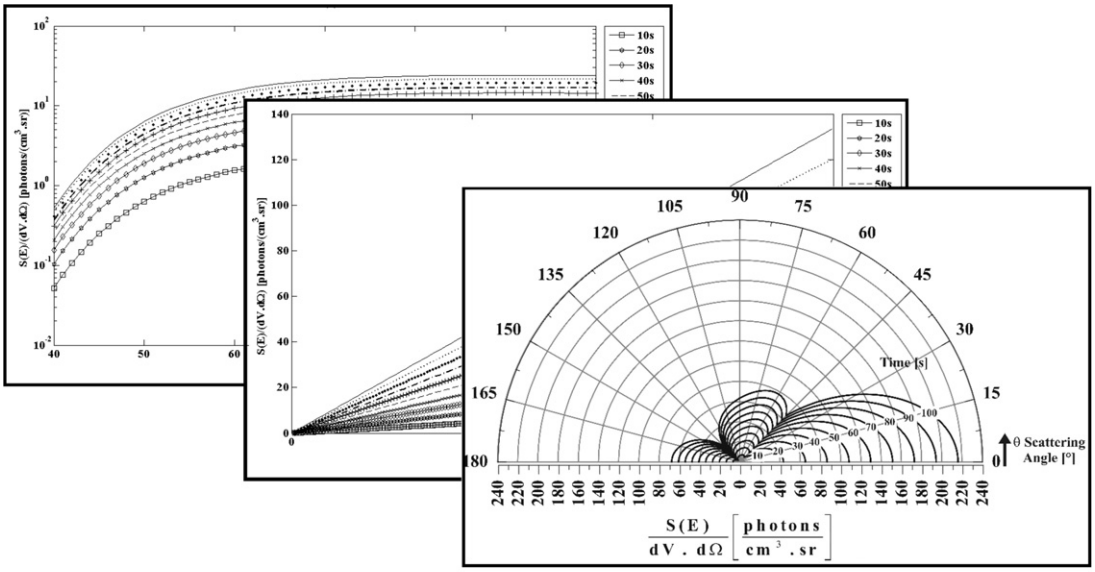

Table 1. Statistical parameters of the results obtained by varying the scattering angle for a time window of 20s: variance (σ_d^2), standard deviation (σ_d) and coefficient of variation (CV).

Statistical Parameters	Energy (E_0) [keV] & Incident Photon Flux (Φ_0) [photons/(s.cm²)]			
	$E_0 = 50$		$E_0 = 100$	
	$\Phi_0 = 15$k	$\Phi_0 = 150$k	$\Phi_0 = 15$k	$\Phi_0 = 150$k
σ_d^2	1,09	109,05	7,53	752,67
σ_d	1,04	10,44	2,74	27,43
CV	64%	64%	42%	42%

Fig. 3. Graphical display produced by the simulation model including the statistical information.

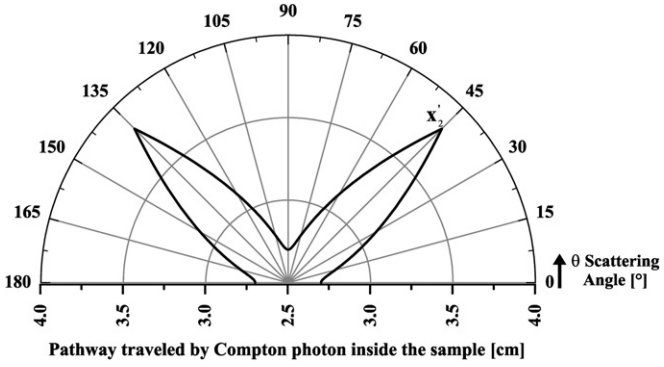

Fig. 4. Graphical output to evaluate the variation of the distance traveled by the Compton photon (x_2') within the sample according to the scattering angle (θ).

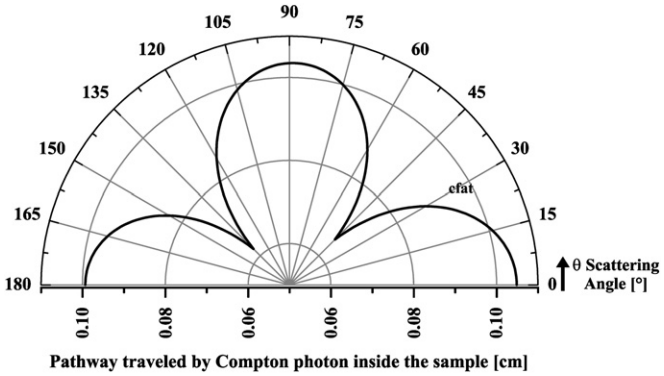

Fig. 5. Graphical output to evaluate the variation of the linear attenuation coefficient factor (*cfat*) versus scattering angle (θ).

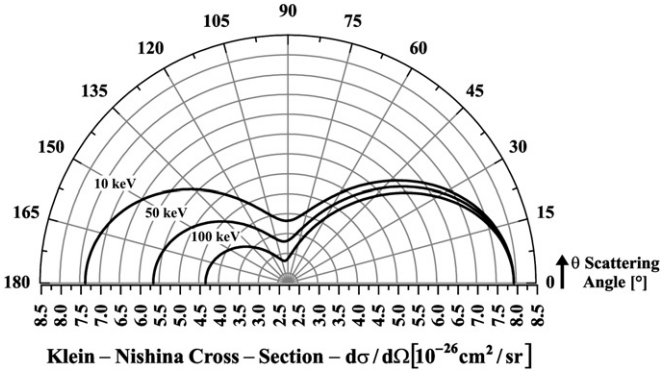

Fig. 6. Graphical output to evaluate the variation of Klein–Nishina cross-section according to the scattering angle (θ).

phantom diagonals divides the graphic into three distinct regions: the first from 0° to 45°, the second, from 45° to 135° and the third, 135° to 180°. The non-similarity of the graphic is due to the different distances traveled by incident and scattered photons, besides their respectively linear attenuation coefficients.

The scattering angle variation influenced the Klein–Nishina cross-section, as depicted in the graphical output of Fig. 6. This output shows the incident energy and the scattering angle variation influenced the Klein–Nishina cross-section amplitude. The amplitude was inversely proportional to the incident photon energy E_0 by the increase of variable α, as predicted by Eq. (15).

It is important to mention that, depending on the scattering angle, the position of the detector influences the scattered photon energy (E), the Klein–Nishina cross-section and the linear attenuation coefficient (μ_2) for the scattering energy. Thus, the analysis by Compton scattering, especially concerning attenuation, can be

divided into two stages: before and after the scattering. For a given incident energy, the interaction of radiation with the matter may present a predominance of the Compton effect before the collision of the electron and the photon. After that, the photoelectric effect becomes predominant due to the energy loss suffered by the photon.

The graphical outputs of the scattering angle variation (Fig. 7) are some examples of the several graphics generated by the simulation process for all energy and initial photon flux range used. Comparing Figs. 5 and 7, it is evident that there is a strong influence of the linear attenuation coefficient on the final result of the amount of scattered photons, seen from the scattering angle variation perspective. The inflection points at 45° and 135° (Fig. 5) can also be seen in Figs. 7(a) and (b). These points represent the longest distance traveled by the scattered photon within the sample (Fig. 4). In this situation, distance x_2' reaches its maximum and, as *cfat* is inversely proportional to x_2', it leads to a reduction in the amount of Compton photons.

Table 1 shows the influence of the scattering angle variation ($\Delta\theta$) on the amount of Compton photons per volume unit (dV) and solid angle unit ($d\Omega$) in terms of statistical parameters, like standard deviation (σ_d), variance (σ_d^2) and coefficient of variation (CV).

For the case study considered, the scattering angle variation ($\Delta\theta$) versus incident energy (E_0) ranging from 50 keV to 100 keV caused a reduction from 64% to 42% in the CV value, respectively. There were no changes in the CV for the same value of E_0 and variation of Φ_0, because the energy variation behaved as a rising exponential function. In other words, for higher values of the energy of incident photons, the variation in the amount of scattered photons is low because the function tends to be stabilized with high values of E_0. For a same value of E_0, there was no change in the CV value related to the variation of Φ_0, since it behaved linearly.

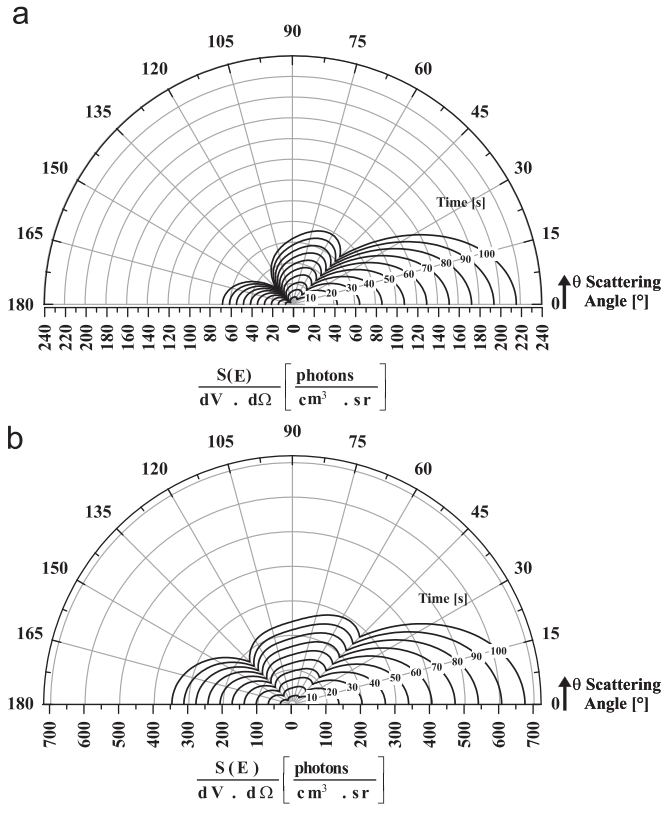

Fig. 7. Graphical output to evaluate the detection of the amount of Compton photons normalized to both volume unit (dV) and solid angle unit ($d\Omega$) as a function of the scattering angle (θ) for different time windows and initial flux of 150 k [photons/(s cm^2)]: (a) incident photon energy of 50 keV and (b) incident photon energy of 100 keV.

Table 1
Statistical parameters of the results obtained by varying the scattering angle for a time window of 20 s: variance (σ_d^2), standard deviation (σ_d) and coefficient of variation (CV).

Statistical Parameters	Energy (E_0) [keV] & incident photon flux (Φ_0) [photons/(s cm^2)]			
	E_0=50		E_0=100	
	Φ_0=15 k	Φ_0=150 k	Φ_0=15 k	Φ_0=150 k
σ_d^2	1.09	109.05	7.53	752.67
σ_d	1.04	10.44	2.74	27.43
CV	64%	64%	42%	42%

The examples of outputs to evaluate the influence of energy variation on the amount of scattered photons are illustrated in Fig. 8.

Concerning the energy variation of incident photons, the probability of detecting Compton photons for angles of 30°, 90° and 120° and flux values of incident photons of 1 k, 15 k and 150 k was evaluated and simulated. The examples of graphical outputs generated for the energy range between 40 keV and 100 keV are illustrated in Fig. 8. It is possible to observe the exponential behavior of the count of scattered photons per volume unit and solid angle unit concerning the energy variation of incident photons. Such behavior was due to the influence that incident energy E exerted on the scattering energy E_0 and also over the linear attenuation coefficients μ_1 and μ_2. These coefficients presented a negative exponential behavior due to the increase in the photon energy and because the variable *cfat* was inversely proportional to this increase. This behavior is reflected in the final result. Besides the linear attenuation coefficient, the incident energy also influenced the Klein–Nishina cross-section inversely, as shown in Fig. 6.

Table 2 shows the influence of the energy variation of incident photons on the amount of scattered photons per volume unit (dV) and solid angle unit ($d\Omega$) in terms of statistical data such as standard deviation (σ_d), variance (σ_d^2) and coefficient of variation (CV).

The information presented in Table 2 shows that there was an increasing variation in the CV value due to the scattering angle variation in the energy range of E_0 for the interval between 40 keV and 100 keV. This variation is shown in Fig. 7, in which the asymmetric variation is directly proportional to the increased angle process. For the same value of θ, the variation of Φ_0 did not change the value of CV and kept the same angular range previously shown.

The graphical output examples illustrated in Fig. 9 and obtained by varying the flux of incident photons clearly illustrate its direct proportionality in the detection of scattered photons. There was a linear behavior in Compton photons detection per volume unit and solid angle unit, in which the Compton photon variation was directly proportional to the increase of the incident photon flux. Such behavior is easily explained since the photons detected by Compton scattering are products of collision of incident photons with electrons in the outer layer of the atom.

Table 3 illustrates the influence of the incident photon flux variation on the amount of scattered photons per volume unit (dV) and solid angle unit ($d\Omega$) concerning statistical parameters like standard deviation (σ_d), variance (σ_d^2) and coefficient of variation (CV).

The results presented in Table 3 show that the variation of the incident photon flux did not influence the value of CV (57%) after the angle and energy modifications. As predicted by Eq. (17),

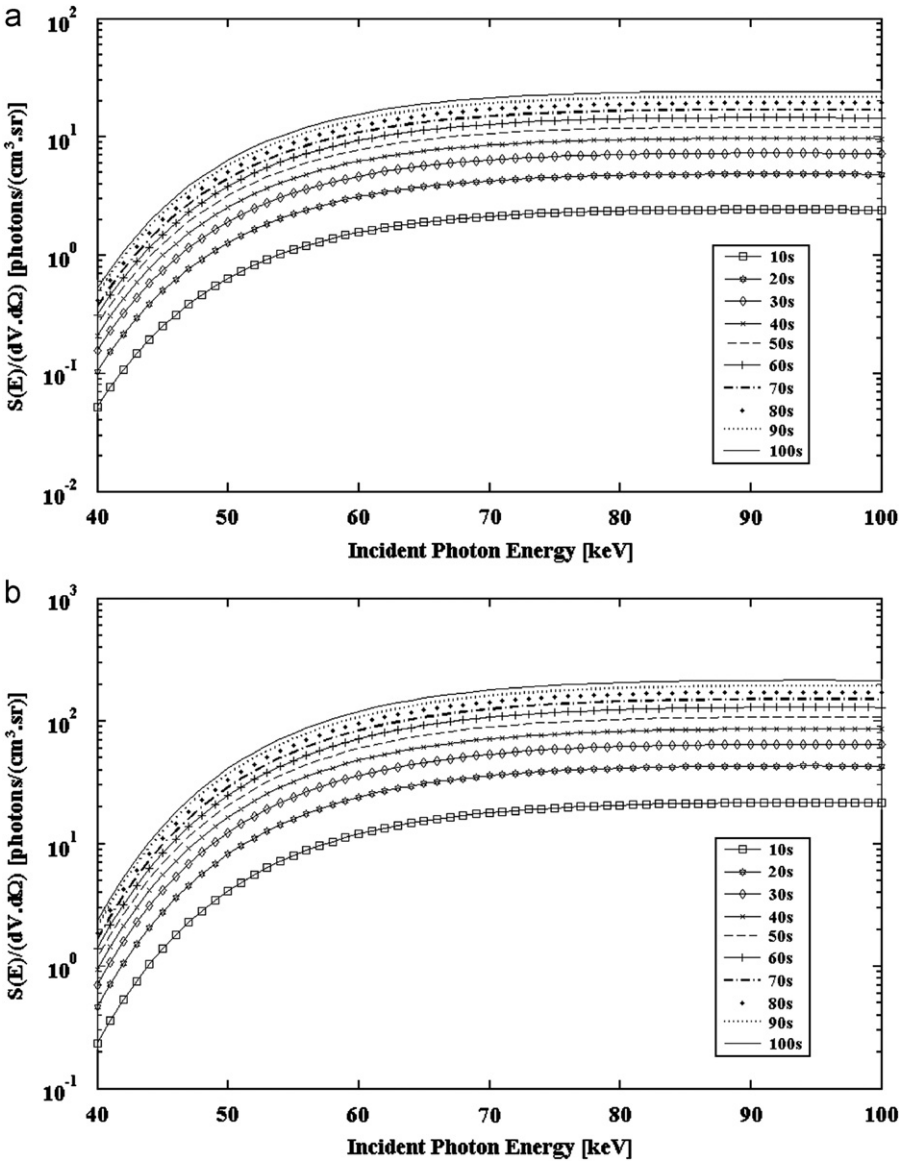

Fig. 8. Graphical output to evaluate the detection of the amount of Compton photons normalized to both volume unit (dV) and solid angle unit ($d\Omega$) versus energy variation of incident photons (40–100 keV) through semi-logarithmic graphics and different time windows: (a) scattering angle of 90° and initial flux of 15 k [photons/(s cm^2)] and (b) scattering angle of 120° and initial flux of 150 k [photons/(s cm^2)].

Table 2
Statistical parameters of the results obtained by varying the incident photon energy for a time window of 20 s: variance (σ_d^2), standard deviation (σ_d) and coefficient of variation (CV).

Statistical Parameters	Scattering Angle (θ) [°] & incident photon flux (Φ_0) [photons/(s cm^2)]					
	$\theta=30°$		$\theta=90°$		$\theta=120°$	
	$\Phi_0=15$ k	$\Phi_0=150$ k	$\Phi_0=15$ k	$\Phi_0=150$ k	$\Phi_0=15$ k	$\Phi_0=150$ k
σ_d^2	9.10	910.18	2.56	255.49	2.29	229.33
σ_d	3.02	30.17	1.60	15.98	1.51	15.14
CV	45%	45%	46%	46%	52%	52%

the variation of the incident photon flux directly influenced the result. On the other hand, the values of θ and E_0 influenced the results of the dependent variables, as *cfat* and *KN*.

Additionally, the graphical output shows that, for some configurations of angle, energy, flux and time window, there was no detection of photons. Table 4 depicts the parameter configuration in which it is possible to detect at least one photon scattered by the Compton effect. Furthermore, for the given boundary conditions it is possible to notice that the incident photon energy to detect at least one photon scattered by the Compton effect presents a direct proportionality to the scattering angle (θ) and an inverse proportionality to the incident photon flux (Φ_0).

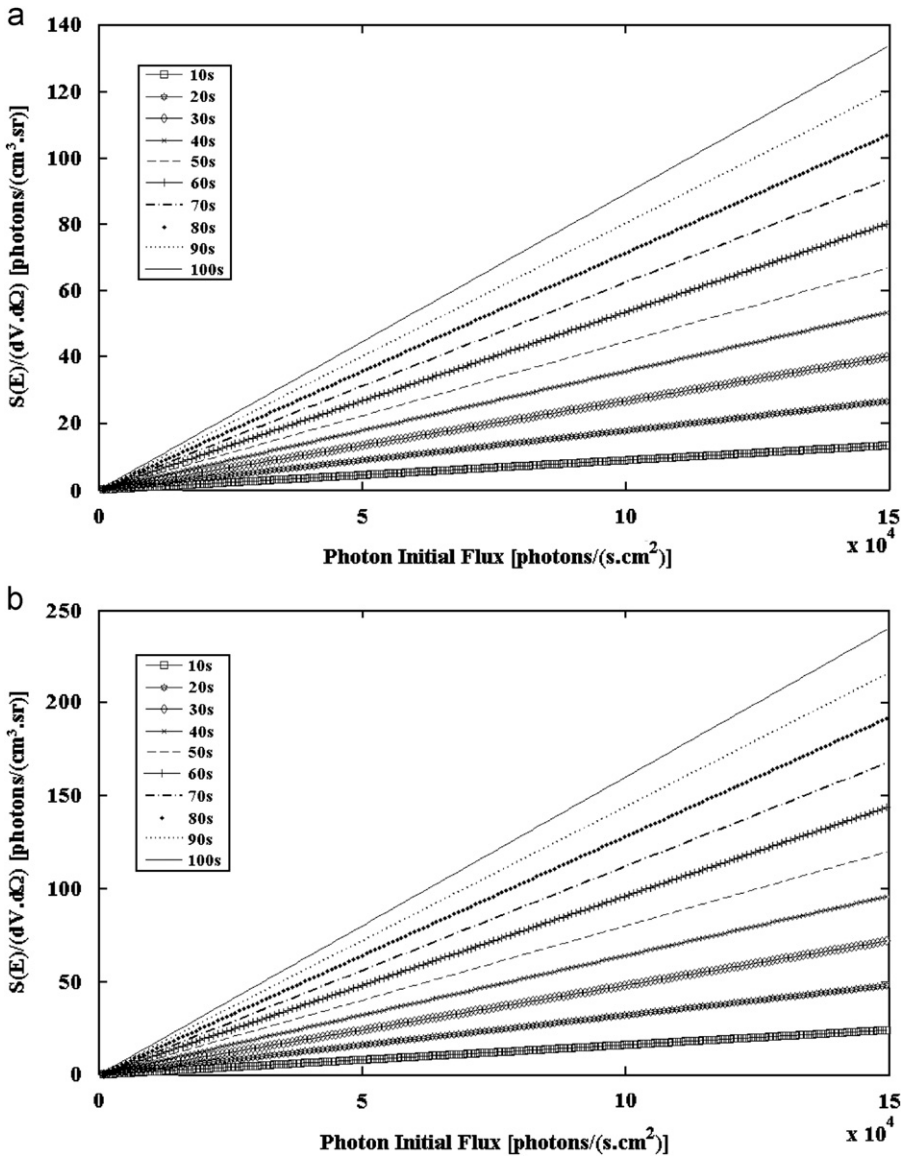

Fig. 9. Graphical output to evaluate the detection of the amount of Compton photons normalized to both volume unit (dV) and solid angle unit ($d\Omega$) versus variation of incident photons flux (1 k–150 k [photons/(s cm^2)]) for different time windows: (a) scattering angle of 30° and 50 keV incident photon energy and (b) scattering angle of 90° and 100 keV incident photon energy.

Table 3
Statistical data of the results obtained by varying the flux of incident photons for a time window of 20 s: variance (σ_d^2), standard deviation (σ_d) and coefficient of variation (CV).

Statistical Parameters	Scattering angle (θ)[°] & energy (E_0) [keV]					
	$\theta=30°$		$\theta=90°$		$\theta=120°$	
	$E_0=50$	$E_0=100$	$E_0=50$	$E_0=100$	$E_0=50$	$E_0=100$
σ_d^2	59.44	718.27	13.30	191.56	5.53	151.63
σ_d	7.71	26.80	3.65	13.84	2.35	12.31
CV	57%	57%	57%	57%	57%	57%

4. Conclusions

The graphical output produced by the tool allows visualizing the influence of the scattering angle and some parameters, such as energy and incident photon flux on the final result of Compton scattering. The output also allows observing how the incident photon flux (Φ_0) generates a linear variation in the detected Compton photons, due to its isolated impact, as predicted by Eq. (19). On the other hand, it is also possible to evaluate independent variables, such as scattering angle (θ) and energy of incident photons (E_0), and how they are related with the nonlinear nature influence on the Compton scattering. Such influence can happens due to the impact of the Klein–Nishina differential cross-section and the factor regarding the linear attenuation coefficients that can be considered in the experimental arrangements, whose variation follows a decreasing exponential.

The case study showed that the scattering angle variation for a 50 keV energy was the assessment parameter to detect the amount of Compton photons that presented the highest coefficient of variation (CV), i.e., 64%. The explanation lies in the exponential nature of the linear attenuation coefficient function, in which its variation increases as the incident photon energy decreases. For the boundary conditions considered, the minimum value of the incident energy to detect at least one Compton photon was 35 keV. Such detection energy can be lower if better

Table 4
Incident Energy (E_0) values [keV] in which it is possible to detect at least one Compton photon per volume unit and per solid angle unit [photon/(cm^3.sr)].

Time window [s]	Incident photon flux (Φ_0) [photons/(s cm^2)] & scattering angle (θ) [°]								
	Φ_0=1 k			Φ_0=15 k			Φ_0=150 k		
	θ=30°	θ=90°	θ=120°	θ=30°	θ=90°	θ=120°	θ=30°	θ=90°	θ=120°
10	–	–	–	48.2	54.0	57.5	39.7	41.8	43.9
20	–	–	–	44.7	48.5	51.3	38.2	39.8	41.9
30	–	–	–	43.2	46.3	48.8	37.4	39.0	40.8
40	65.5	–	–	42.3	45.0	47.4	36.9	38.3	40.2
50	59.5	–	–	41.5	44.1	46.5	36.5	37.9	39.7
60	56.3	–	–	41.0	43.4	45.7	36.2	37.5	39.3
70	54.3	70.5	91.0	40.6	42.9	45.2	35.9	37.2	39.0
80	53.0	65.0	73.0	40.0	42.5	44.5	35.7	37.0	38.8
90	51.9	61.6	67.6	39.5	42.1	44.2	35.6	36.8	38.5
100	51.8	59.4	64.6	39.7	41.7	43.8	35.4	36.6	38.3

detectors are used in the photopeak region, presenting better efficiency and resolution in energy.

The Compton effect can support the characterization of physical quantities of a given sample and be applied to medicine, industry, agriculture and other areas of knowledge. The information presented in this paper was useful for comparisons and evaluations of laboratory measurements using the Compton scattering in studies of agricultural soil compaction. Additionally, such strategy will allow validating a computational model that deals with the scattering of photons by the Compton effect and dedicated instruments that have been implemented at Embrapa Instrumentation.

Acknowledgments

The authors would like to acknowledge Embrapa Agricultural Instrumentation Center (Project MP3 process 03.10.05.011.00.00), the Physics Institute of São Carlos - IFSC and São Paulo Research Foundation - FAPESP for the financial support (process 09/50405-1) given to this research.

References

[1] H. Hertz, Ann. Phys. 31 (1887) 983.
[2] A. Einstein, Ann. Phys. 17 (1905) 891.
[3] H.A. Jahagirdar, et al., Appl. Radiat. Isot. 44 (1993) 875.
[4] A.H. Compton, Phys. Rev. 21 (1923) 483.
[5] A.T. Young, Appl. Opt. 20 (1981) 533.
[6] A.L. Hanson, Nucl. Instr. Meth. Phys. Res. A 234 (1985) 552.
[7] J. Chadwick, M. Goldhaber, Nature 134 (1934) 237.
[8] M.B. Chadwick, Nucl. Phys. A 654 (1999) 1051c.
[9] R. Cesareo, et al., Appl. Radiat. Isot. 45 (1994) 613.
[10] O. Klein, Y. Nishina, Z. Phys. 52 (1929) 853.
[11] O. Klein, Y. Nishina, in: H.A. Bethe, A.H. Guth (Eds.), On the scattering of radiation by free electrons, World Scientific Publishing Co. Pte. Ltd., Singapore, 1994, pp. 113–139.
[12] S. Chen, M. Kotlarchyk, Interaction of Photons and Neutrons with Matter, second ed., World Scientific, New Jersey, 1999.
[13] A.L. Hanson, et al., Phys. Rev. Lett. 61 (1988) 135.
[14] A.L. Hanson, G.E. Gigante, Phys. Rev. A 40 (1989) 171.
[15] G.E. Gigante, A.L. Hanson, Nucl. Instr. Meth. Phys. Res. A 280 (1989) 299.
[16] R. Cesareo, et al., Phys. Rep. 213 (1992) 117.
[17] T.H. Prettyman, et al., Appl. Radiat. Isot. 44 (1993) 1327.
[18] F.A. Balogun, N.M. Spyrou, Nucl. Instr. Meth. Phys. Res. B 83 (1993) 533.
[19] S.J. Norton, J. Appl. Phys. 16 (1994) 2007.
[20] G. Harding, Radiat. Phys. Chem. 50 (1997) 1997.
[21] J.H. Hubbell, Radiat. Phys. Chem. 50 (1997) 113.
[22] F.A. Balogun, Appl. Radiat. Isot. 50 (1999) 317.
[23] F.A. Balogun, et al., Radiat. Phys. Chem. 59 (2000) 23.
[24] P.E. Cruvinel, F.A. Balogun, XIII SIBGRAPI, 17–20, Gramado. In Proc. IEEE Comp. Soc., 193–199, 2000.
[25] P. Yalçin, et al., Radiat. Phys. Chem. 58 (2000) 325.
[26] R. Cesareo, et al., Radiat. Phys. Chem. 61 (2001) 339.
[27] R. Cesareo, et al., Nucl. Instr. Meth. Phys. Res. A 487 (2002) 188.
[28] F.A. Balogun, P.E. Cruvinel, Nucl. Instr. Meth. Phys. Res. A 505 (2003) 502.
[29] S. Agostinelli, et al., Nucl. Instr. Meth. Phys. Res. A 506 (2003) 250.
[30] S.C. Roy, R.H. Pratt, Radiat. Phys. Chem. 69 (2004) 193.
[31] Ö. Söğüt, et al., J. Quant. Spectrosc. Radiat. Transfer 87 (2004) 15.
[32] D. Rao, et al., Radiat. Phys. Chem. 70 (2004) 479.
[33] T. Çonka-Nurdan, et al., IEEE Trans. Nucl. Sci. 52 (2005) 1381.
[34] P.E. Cruvinel, F.A. Balogun, Rev. Eng. Agríc. 26 (2006) 151.
[35] S. Pašić, K. Ilakovac, Radiat. Phys. Chem. 75 (2006) 1683.
[36] M. Donativi, et al., Nucl. Instr. Meth. Phys. Res. B 264 (2007) 189.
[37] H. Seo, et al., Nucl. Instr. Meth. Phys. Res. A 580 (2007) 314.
[38] H. Seo, et al., Nucl. Instr. Meth. Phys. Res. A. 591 (2008) 80.
[39] W. Yao, K. Leszczynski, Med. Phys. 36 (2009) 3145.
[40] F.V. Hartemann, Nucl. Instr. Meth. Phys. Res. A 608 (2009) S1.
[41] R.H. Pratt, et al., Radiat. Phys. Chem. 79 (2010) 124.
[42] L.F. Pires, et al., Soil Till. Res. 110 (2010) 197.
[43] M.J. Berger, J.H. Hubbell, XCOM: photon cross-sections on a personal computer, National Institute of Standards and Technology (1987).